Journal of Computational Physics 228 (2009) 903–920

Contents lists available at ScienceDirect

Journal of Computational Physics

journal homepage: www.elsevier.com/locate/jcp

Immersed boundary method for the MHD flows of liquid metals

D.G.E. Grigoriadis, S.C. Kassinos *, E.V. Votyakov

Computational Science Laboratory UCY-CompSci, Department of Mechanical and Manufacturing Engineering, University of Cyprus, 75 Kallipoleos, Nicosia 1678, Cyprus

ARTICLE INFO

Article history:
Received 8 February 2008
Received in revised form 28 June 2008
Accepted 5 October 2008
Available online 1 November 2008

Keywords:
MHD flow
Incompressible flow
Circular cylinder
Immersed boundary method
Conducting fluid
Complex geometries

ABSTRACT

Wall-bounded magnetohydrodynamic (MHD hereafter) flows are of great theoretical and practical interest. Even for laminar cases, MHD simulations are associated with very high computational cost due to the resolution requirements for the Hartmann and side layers developing in the presence of solid obstacles. In the presence of turbulence, these difficulties are further compounded. Thus, MHD simulations in complex geometries are currently a challenge. The immersed boundary (IB hereafter) method is a reliable numerical tool for efficient hydrodynamic field simulations in arbitrarily geometries, but it has not yet been extended for MHD simulations. The present study forms the first attempt to apply the IB methodology for the computation of both the hydrodynamic and MHD fields. A consistent numerical methodology is presented that is appropriate for efficient 3D MHD simulations in geometrically complicated domains using cartesian flow solvers. For that purpose, a projection scheme for the electric current density is presented, based on an electric potential correction algorithm. A suitable forcing scheme for electric density currents in the vicinity of non-conducting immersed surfaces is also proposed. The proposed methodology has been first extensively tested for Hartmann layers in fully-developed and developing channel and duct flows at Hartmann numbers $Ha = 500 - 2000$. In order to demonstrate the potential of the method, the three-dimensional MHD flow around a circular cylinder at Reynolds number $Re = 200$ is also presented. The effects of grid resolution and variable arrangement on the simulation accuracy and consistency were examined. When compared with existing numerical or analytic solutions, excellent agreement was found for all the cases considered. The proposed projection and forcing schemes for current densities were found capable of satisfying the charge conservation law in the presence of immersed non-conducting boundaries. Finally, we show how the proposed methodology can be used to extend the applicability of existing flow solvers that use the IB concept with a staggered variable arrangement.

1. Introduction

The capability to accurately simulate flows in complex geometries is one of the key current issues in computational MHD flows. For example, many engineering problems related to the conceptual design of fusion reactors involve complicated geometrical domains [1]. In the self-cooled liquid metal fusion blanket, a circulating, highly conducting, liquid metal is used as coolant and breeder material. The interaction of this moving liquid conductor and the magnetic field confining the plasma is likely to suppress turbulence, whereas the demand for high heat transfer rates favors a turbulent or at least a time-dependent flow. Beside other possibilities, described for example in Buhler [2] or Moreau [3], an obvious way to enhance mixing

* Corresponding author. Tel.: +357 22892296; fax: +357 22892254.
E-mail addresses: kassinos@ucy.ac.cy, s_kassinos@yahoo.com (S.C. Kassinos).

0021-9991/$ - see front matter © 2008 Elsevier Inc. All rights reserved.
doi:10.1016/j.jcp.2008.10.017

and heat transfer in an electrically insulated channel is through cylindrical obstacles, so called turbulence promoters, which are aligned with the magnetic field. This concept has been investigated experimentally [4–6] and numerically [7–10].

Simulations of MHD problems are by definition computationally more intensive as compared to purely hydrodynamic problems. First of all, apart from flow phenomena like turbulence which might coexist for weak magnetic fields, the consistent inclusion of the Lorentz force involves the solution of an extra full poisson equation in order to satisfy the charge conservation law. Additionally, when intense external magnetic fields are applied, Hartmann layers are formed close to solid boundaries with a thickness inversely proportional to the intensity of the wall-normal magnetic field [3]. At high Hartmann numbers, the thickness of these boundary layers is drastically reduced. Therefore, the application of any computational method in wall-bounded MHD flows is always complicated by the need to adequately resolve the Hartmann layers. This requirement resembles the Reynolds number restriction faced in direct and large-eddy simulations (DNS and LES) of hydrodynamic flows, where turbulent boundary layers become increasingly thinner as the Reynolds number is increased. However, in the hydrodynamic case, wall models [11] and Hybrid LES–RANS methods [12] have been developed that can help to avoid the – expensive – numerical resolution of these areas, at least for LES calculations. In MHD flows however, although such models have been developed [13,14] for simplified cases, they have not been systematically applied and examined up to now.

In the absence of a systematic and well-established general modeling procedure amounting to an effective "wall model for Hartmann layers", one has to resolve these layers numerically. Proper grid refinement close to solid bodies at high Ha numbers, results in a high computational cost, therefore, an efficient and accurate numerical method for wall-bounded MHD flows in complicated geometries is a necessity.

The numerical treatment of MHD flows in geometrically complicated domains has sofar relied on the use of unstructured or boundary-fitting curvilinear grids [8–10]. Using an exponential polar grid, Mutschke et al. [8] studied the effect of magnetic field direction for the liquid metal flow around a circular cylinder. Recently, Sekhar et al. [9] used a multigrid method with polar grids to examine the same MHD flow configuration at high Ha numbers and at $Re_d = 100 - 500$, where Ha and Re_d numbers were defined based on the free stream velocity and the cylinder's diameter d.

Non-boundary-conforming methods, which are often a very efficient choice for simulations in complicated domains, have not yet been extended for MHD flows. These methods were initially proposed and applied for direct and large-eddy simulations (DNS and LES) of turbulent flows, where computational efficiency and accuracy are imperative. Most of them take advantage of the efficiency and robustness of Cartesian or cylindrical coordinate solvers, achieving a reduced computational cost per node. Especially for cases where increased numerical resolution is a key issue, non-boundary-conforming methods can lead to significant performance gains.

Several computational approaches exist that can be classified as non-boundary-conforming methods. First formulated by Peskin [15], the IB method was the first attempt to represent a flow obstruction or a solid interface by a set of discrete forces. Since then various modifications to the method have been proposed, leading to schemes based on a feedback-forcing scheme [16], cut-cell approaches [17], or ghost-cell methods [18] and imbedded-boundary methods [19]. An extensive review of the present state of the IB method, and the associated difficulties, can be found in [20]. The main advantages of the IB method, when compared to boundary-fitting curvilinear or unstructured grid methods, are memory and CPU savings as well as ease of grid generation [21,22]. When combined with the efficiency of direct pressure solvers, IB methods can reveal their full potential for efficient and accurate simulations in complicated geometries [23].

In the IB method, a cartesian or cylindrical grid solver is used and discrete momentum forcing is applied in the Navier–Stokes equations to dynamically represent the location and characteristics of the solid boundaries [19,24,25]. As a result, flows in complicated domains, including moving and deforming boundaries, can be handled with simple orthogonal, cartesian grids that may not coincide with solid boundaries. The IB method has been successfully used so far in hydrodynamic simulations, eliminating the need for body fitting domains, complicated grid generation or remeshing [25]. Recently, Yang and Balaras [20] and Balaras [26] proposed an imbedded-boundary computational procedure that is capable of simulating turbulent flows with stationary or moving boundaries.

The approach adopted in the present study, can be classified as a *discrete forcing* approach in terms of immersed boundary methodology [27], i.e. a discrete forcing field is used to impose the boundary conditions along immersed surfaces. Although it shares some similarities with the *ghost-cells* and *cut-cell* methods, the present approach follows the schemes suggested in [20] and [26]. The imbedded-boundary formulation is extended to account for the electric current density field using direct discrete forcing and local field reconstruction in order to satisfy the charge conservation law with immersed surfaces.

The present study is motivated by the belief that the IB method could bring to MHD simulations the same advantages it offers for hydrodynamic cases, especially in regions where thin boundary layers around complicated geometries have to be resolved. The use of the IB method simplifies grid design and could offer adequate resolution for high Hartmann number flows at a reasonable cost. Hence it has the potential to extend the range of computable wall-bounded MHD flows significantly.

The main objective of the present study is to develop an efficient immersed boundary methodology suitable for complicated three-dimensional MHD flows and to demonstrate the ability of the method to accurately represent all the important flow features. In order to verify the accuracy of the proposed method, suitable test cases have been considered that contain all the relevant flow patterns. Steady and unsteady flows in channels, ducts and over a circular cylinder are investigated under various magnetic field intensities and directions.

In the following sections, the theoretical formulation for the MHD flow of an incompressible conducting fluid is first presented. The numerical methodology adopted is then introduced together with the extension of the IB method for MHD flows

at low magnetic Reynolds numbers. The study focuses especially on a consistent and conservative numerical method for the calculation of the electric potential and the current density field around immersed surfaces using the IB concept. Finally, computational results and comparisons with available data are presented and discussed. The applicability of the method to more complicated flows, and issues related to the numerical resolution and computational cost, are also discussed.

2. Governing equations

We consider an incompressible fluid of density ρ, molecular viscosity μ, dynamic viscosity $\nu = \mu/\rho$ and electric conductivity σ, flowing with velocity u_∞. A uniform externally applied magnetic field of intensity b_o is imposed in an electrically insulated domain Ω, with a characteristic length dimension d. Assuming that the magnetic Reynolds number $Re_m = \mu^* \sigma u_\infty d$ (where μ^* is the magnetic permeability) is smaller than unity, the induced magnetic field is expected to be weak in magnitude when compared to the externally applied field, and can be neglected. Under these conditions, the flow under investigation is completely described by the set of Navier–Stokes equations for an isothermal and conductive incompressible fluid. Using d and u_∞ as the characteristic length and velocity scales, scaling the magnetic field intensity with B_o and the electric field and current density by $u_\infty B_o$, the non-dimensional form of the continuity and momentum equations become,

$$\nabla \cdot \vec{u} = 0 \tag{1}$$

$$\frac{\partial \vec{u}}{\partial t} + (\vec{u} \cdot \nabla)\vec{u} = -\nabla p + \frac{\nabla^2 \vec{u}}{Re_d} + N(\vec{J} \times \hat{b}_o) + \vec{f}_{u,IB}, \tag{2}$$

where $\vec{f}_{u,IB}$ is the modified body force related to the IB method for the momentum [28], $\hat{b}_o$ is the unit vector of the applied magnetic field and $\vec{F}_L = N(\vec{J} \times \hat{b}_o)$ is the Lorentz force. In the absence of Hall effects, the non-dimensional electric current density $\vec{J}$ is given by Ohm's law,

$$\vec{J} = \vec{E} + \vec{u} \times \hat{b}_o + \vec{f}_{j,IB}, \tag{3}$$

where $\vec{E}$ is the produced electric field and the term $\vec{f}_{j,IB}$ is the externally imposed current density field associated with the IB method (explained in detail in Sections 3.2 and 3.3). The main dimensionless groups involved are the hydrodynamic Reynolds number Re_d, and the magnetic interaction parameter N (or Stuart number),

$$Re_d = \frac{u_\infty d}{\nu} \quad \text{and} \quad N = \frac{\sigma B_o^2 d}{\rho u_\infty}, \tag{4}$$

where σ is the magnetic resistivity of the medium. Stuart number N expresses the ratio of Lorentz forces over inertia forces. The derived Hartmann number Ha, describing the ratio of Lorentz forces over viscous forces, is then

$$Ha = \sqrt{Re_d N} = dB_o \sqrt{\frac{\sigma}{\rho \nu}}. \tag{5}$$

3. Numerical methodology

In the majority of hydrodynamic simulations, the solution of the involved poisson equation for the pressure is usually achieved by iterative (ADI, SOR, Multigrid, etc.) solvers, that consume a major fraction of the total computational effort. In the quasi-static limit, the MHD approximation involves the inclusion of an extra force term $N(\vec{J} \times \hat{b}_o)$ in the N–S Eqs. (12), which might intuitively seem like a small overhead in computational effort. However, hidden behind this term is the need to solve an extra poisson equation for the electric potential at each computational cycle. Thus, it should be noted that the additional computational effort implied by the inclusion of MHD effects is quite significant.

Consider for example a typical hydrodynamic simulation that consumes a fraction of computational cost γ (which is usually in the range 30–80%) for each poisson solution. For a similar MHD simulation, the cost would then be expected to increase at least by a factor of $(1+\gamma)$ just due to the extra poisson solution required at each computational cycle. Therefore, efficient numerical methodologies, especially for poisson solutions are even more important in MHD simulations. Direct pressure solvers can meet these requirements, since they are fast, efficient and parallelizable numerical algorithms for the solution of the Poisson's equation [29–31]. However, they are by nature restricted to orthogonal or cylindrical domains without internal boundaries. As will be shown later, that disadvantage is completely eliminated by the use of the IB method, which allows the specification of complicated, deforming, or even moving boundaries within rectangular domains using simple cartesian grids.

3.1. Cartesian flow solver

The basic cartesian flow solver used for the present study uses a second order finite-difference scheme for the spatial discretisation on orthogonal grids with a staggered variable arrangement [23,28]. The Navier–Stokes Eq. (2) for a conductive incompressible fluid under the influence of a constant magnetic field $\hat{b}_o$ are solved numerically using the fractional time step

approach [23,28,32]. Time advancement is based on a time-splitting, fully explicit projection scheme with pressure correction. In descretised form, the Navier–Stokes equations are considered in dimensionless form,

$$\vec{u}|^{n+1} = \vec{u}|^{n} + \Delta t[\alpha H(u)|^{n} + \beta H(u)|^{n-1} - \nabla p|^{n+1}] \quad \text{with } H(u)|^{n} = -(\vec{u}\cdot\nabla)\vec{u}|^{n} + \frac{\nabla^2\vec{u}}{Re_d}\Big|^{n} + N(\vec{J}\times\hat{b}_o)|^{n} + \vec{f}_{u,IB}|^{n}, \tag{6}$$

where the superscript denotes the time level and the operator $H(u)$ contains all the convective, viscous and Lorentz force terms. The last term $\vec{f}_{u,IB}$, denotes the immersed boundary forcing term for the momentum. It is used to drive the velocity field to the desired value at the immersed boundaries Γ of the domain in accordance to the procedure described by Balaras in [26]. In practice, momentum forcing is applied in the discrete sense by a proper definition of the term $\vec{f}_{u,IB}$ for the velocity nodes adjacent to the solid interface. Comparisons with analytical solutions and accurate spectral simulations of hydrodynamic flows reported in [26], clearly demonstrated the retainment of second order accuracy close to solid boundaries.

The coefficients α, β define the type of explicit scheme used. For the second order accurate Adams–Bashforth scheme used here, these are simply 3/2 and −1/2, respectively. Assuming that all properties at time level n are known, the first step of the time-splitting scheme is realised by defining a provisional momentum field, using the fully explicit Adams–Bashforth scheme for all terms,

$$\vec{u}|^{*} = \vec{u}|^{n} + \Delta t\left[\frac{3}{2}H(u)|^{n} - \frac{1}{2}H(u)|^{n-1} - \nabla p|^{n}\right], \tag{7}$$

which does not satisfy continuity. Mass conservation at level $n+1$, i.e. the condition $\nabla\cdot\vec{u}^{n+1} = 0$, is imposed by the solution of a poisson equation for pressure correction δp [32] according to,

$$\nabla^2\delta p = \frac{\nabla\cdot\vec{u}^{*}}{\Delta t}, \tag{8}$$

which is solved using a direct pressure solver. In the case of Dirichlet boundary conditions for the velocity field, the consistent boundary conditions for the pressure along the immersed boundary Γ are $\nabla(\delta p)\cdot\vec{n} = 0$, which is satisfied for the present formulation as shown in [26]. The last projection step is realised by updating the variables for the next time level,

$$\vec{u}|^{n+1} = \vec{u}|^{*} - \Delta t\nabla\delta p \tag{9}$$

$$p|^{n+1} = p|^{n} + \delta p. \tag{10}$$

Lorentz force terms in Eq. (6) were considered at time level n, which is consistent with the fully explicit nature of the algorithm. Stronger coupling of pressure and Lorentz forces could be possibly achieved by using the Lorentz forces at time level $n+1$. In that case though, pressure boundary conditions would also include contributions from the Lorentz forces, significantly complicating the numerical procedure [33]. The procedure followed for the calculation of the electric current density $\vec{J}$ and the associated Lorentz force are presented in the next section.

3.2. Projection scheme for current density

Calculating current densities involves the estimation of the irrotational electric field $\vec{E}$ of Eq. (3), which is normally expressed in terms of an electrostatic potential as $\vec{E} = -\nabla\Phi$. The electric current density as governed by Ohm's law in a domain Ω, can then be expressed in terms of Φ as,

$$\vec{J} = -\nabla\Phi + (\vec{u}\times\hat{b}_o), \tag{11}$$

where the externally applied magnetic field $\hat{b}_o$ can also be space varying. Using the electric charge conservation law, a solenoidal condition also applies for the electric current density, i.e. $\nabla\cdot\vec{J} = 0$. Thus, a poisson equation can be derived for the electric potential [34] at each time level n,

$$\nabla^2\Phi|^{n} = \nabla\cdot(\vec{u}\times\hat{b}_o)|^{n} = \hat{b}_o\cdot\vec{\omega}|^{n}, \tag{12}$$

where $\vec{\omega} = \nabla\times\vec{u}$ is the fluid vorticity. In the majority of MHD simulations, Eq. (12) is solved at each time step to satisfy electric charge conservation. For boundary-conforming methods, the boundary conditions applied on $\vec{J}$ are imposed directly along the explicitly defined surface Γ. In IB methods, that is not directly possible since the advantage of the method lies in the dynamic representation of immersed surfaces instead of their explicit definition. Additionally, most of the efficient sparse matrix solvers do not allow local modifications of the coefficients involved in the poisson solution algorithm at the internal part of Ω.

In order to alleviate these difficulties, and in analogy with momentum, we propose a formulation for current density that includes a prescribed forcing of the current density field according to

$$\vec{J}|^{n} = -\nabla\Phi|^{n} + (\vec{u}\times\hat{b}_o)^{n} + \vec{f}_{j,IB}|^{n}, \tag{13}$$

where the term $\vec{f}_{j,IB}$ is an externally imposed current density field associated with the IB method. The role of the space and time varying field $\vec{f}_{j,IB}$ is to drive the current density field and the involved electric potential according to the specified boundary condition imposed along the immersed surfaces Γ. In doing so, one can control boundary conditions of $\vec{J}$ along

the immersed bodies, and different magnetic wall conductivities can be considered, from perfect conductors to perfect insulators. For the latter case, the necessity of including such a forcing in IB formulation can be demonstrated. For a non-conducting, stationary surface, the proper boundary condition for the current density and electric potential are $\vec{J}_\Gamma = 0$ and $\partial\Phi/\partial n = 0$ along Γ. Eqs. (11) and (12) do not provide any means of satisfying such conditions and control the behavior of $\vec{J}$ and Φ close to the immersed boundary. Instead, using Eq. (13) and a forcing field of the form,

$$\vec{f}_{j,IB}|^n = \begin{cases} +\nabla\Phi|^n - (\vec{u}\times\hat{b}_o)|^n, & \text{along} \quad \Gamma \\ 0, & \text{otherwise} \end{cases} \tag{14}$$

the desired condition $\vec{J}_\Gamma = 0$ can be imposed. Then, since $u_{i,\Gamma} = 0$, the proper boundary condition for the electric potential along the surface is also recovered, i.e. $\partial\Phi/\partial n = 0$. However, Eqs. (13) and (14) cannot be used as they stand, since the electric potential is also unknown at time level n.

In order to avoid computationally expensive iterative algorithms, a projection scheme for the current density is proposed. In the general case, the current density field can be decomposed to the desired unknown solenoidal field $\vec{J}|^n$ and the gradient of a scalar $\nabla\Phi$. A suitable provisional current density field $\vec{J}|^*$ can then be defined as,

$$\vec{J}|^* = -\nabla\Phi|^{n-1} + (\vec{u}\times\hat{b}_o)^n + \vec{f}_{j,IB}|^n, \tag{15}$$

$$\text{where} \quad \vec{J}|^n = \vec{J}|^* - \nabla\delta\Phi. \tag{16}$$

The forcing term $\vec{f}_{j,IB}|^n$ is the external forcing field that should drive the current density field according to the boundary conditions desired along the immersed boundaries and it is provided by the procedure explained in the next section. Due to the adopted definition, it is clear that the scalar field Φ coincides with the electrostatic potential field. Imposing the solenoidal condition for the field $\vec{J}|^n$ on Eq. (13), so that the charge conservation law at time level n is satisfied, leads to a poisson equation for the electric potential difference $\delta\phi$,

$$\nabla^2\delta\phi = \nabla\cdot\vec{J}|^*, \tag{17}$$

which if satisfied, can restore the solenoidal nature of current density at time level n by correcting the provisional field $\vec{J}^*$ for which $\nabla\cdot\vec{J}^*\neq 0$. Eq. (17) can be solved using a procedure similar to the one used for the pressure solution. In the present study, it was solved directly, using exactly the same direct poisson solver that is used for the pressure correction. Accurate solution of Eq. (17) is crucial and can guarantee the overall accuracy of the current density field by eliminating any charge sources or sinks. As in the case for the momentum correction, the projection of electric current density is completed by,

$$\vec{J}|^n = \vec{J}|^* - \nabla\delta\phi \tag{18}$$

$$\Phi|^n = \Phi|^{n-1} + \delta\phi. \tag{19}$$

3.3. Immersed boundary forcing for current densities

The IB concept is based on the dynamical representation of fluid–solid interfaces. In the present study, these interfaces are defined by a series of line segments, parametric lines, or parametric surfaces in three-dimensions. For simplicity, the analysis here is performed for two dimensions although it was designed and implemented for the three-dimensional space.

These parametric segments $\Gamma(s)$ are originally defined through marker points and a front tracking scheme [20,26]. Then, they are reconstructed in a piecewise fashion using polynomials of second order. Grid nodes are identified using a tagging process by drawing the normal vector from the reconstructed immersed line to each node of the cartesian grid surrounding the specific marker point. Depending on the predefined orientation, the sign of projection or dot product of these vectors along the unit normal identifies if they lie in the solid or the fluid part of the domain (Fig. 1(a)). Grid nodes denoted as *fluid* lie within the fluid part and are solved for, while the *solid* nodes do not contribute to the simulation.

Once the two phases are separated, fluid nodes which have at least one solid neighbor are characterised as *forcing* nodes (F), which are actually the boundary points for the calculation. These forcing nodes do actually couple the numerical solution in the fluid part of the domain with the boundary conditions imposed along any solid interface $\Gamma(s)$. Their properties should be estimated in a consistent way, so that the presence of the immersed surface is mimicked dynamically according to the desired boundary conditions. Therefore, the values imposed at the forcing nodes should consider the surrounding fluid nodes, and the same time, reflect the type of boundary conditions along Γ in the discrete sense. Within the IB methodology this is usually achieved by interpolation schemes, which consider the value on the interface J_Γ and the value at the fluid part of the domain. In the present study, the interpolation to the forcing node considers the value at the closest boundary point J_Γ and that of a *virtual* node J_V located inside the fluid part [20] as shown in Fig. 1(b). The location of the virtual node is defined by projecting the unit normal to the fluid part so that the forcing node bisects the distance ΨV (i.e. $d_1 = d_2$).

Considering Dirichlet boundary conditions, the current density at the forcing nodes J_V can then be computed from a linear interpolation scheme,

$$J_F = \left(\frac{d_2}{d_1+d_2}\right)J_\Gamma + \left(\frac{d_1}{d_1+d_2}\right)J_V. \tag{20}$$

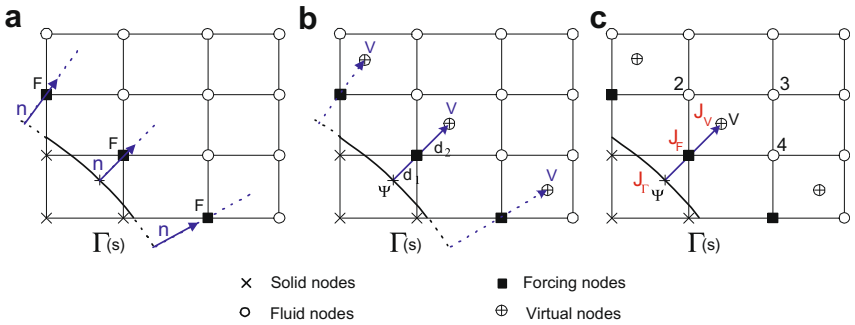

Fig. 1. Phases of the front tracking technique as defined in [20,26]. (a) Distinguishing solid and fluid nodes, identifying forcing nodes (F), (b) defining virtual nodes (V) by projection along the wall-normal vectors and (c) defining the interpolation stencil used for the projected virtual node.

The current density at the virtual node is computed using a simple trilinear interpolation scheme according to,

$$J_V = \sum_{i=1}^{N} \alpha_i J_i, \tag{21}$$

where α_i is the weighting factor of fluid node i and N the total number of fluid nodes considered for the interpolation (fluid nodes 2, 3 and 4 in Fig. 1(c)). In the implementation presented here, a 2×2 stencil has proved to be sufficient for the interpolation to the virtual node. As demonstrated in [20] such a scheme is capable of retaining the second order degree of accuracy close to immersed surfaces.

The current density forcing method described above, forms a consistent numerical algorithm for the forcing procedure defined in Eq. (14). Once applied for all the forcing nodes in the domain, at each time level, it can dynamically mimic the electrostatic definition of any non-conducting immersed surface Γ. With regards to the sources of the poisson equations for the pressure and the electric potential, it should be noted that these should be specified at fluid locations only. Due to the definition of the forcing nodes, they are the last nodes (before the immersed surfaces) that affect the fluid part solution. Hence, the solid nodes do not affect directly the fluid part of the domain, and the sources inside any existing solid sub-domain immersed in Ω do not contribute at all to the simulation. These sources can therefore be defined in any matter without affecting the simulation.

The exact location of the forcing nodes, follows naturally from the definition of variable location. For staggered discretisations like the one presented in Section 3.4.1, the location of each component of current density coincides with the location of the corresponding velocity component. For cell-centered discretisations, (Section 3.4.2), the location of forcing nodes for each component of current density coincides with pressure location. Hence, in both cases, defining the forcing parameters for current densities does not require any extra computational effort for existing IB based flow solvers.

For stationary boundaries, the procedure described above is performed before the main solution and the neighbors of each forcing node and their coefficients α_i with the associated arrays are kept in memory. In the case of moving boundaries, one has to repeat the procedure each time the location of the immersed boundary is redefined. Due to its simplicity, the algorithm is extremely efficient, especially for three-dimensional problems, since the application of forcing requires only a limited number of operations and is easily performed in parallel.

It should be noted, however, that the calculation of surface variables as needed for the calculation of pressure and shear forces around immersed bodies, is not a straight forward task in IB methods. Several methodologies exist for the reconstruction of the solution close to the immersed boundary [35]. In the present work, the methodology described in [20] has been used, since it can be easily generalized and extended for 3D turbulent flows, and is appropriate for moving boundaries. Full details of the reconstruction scheme can be found in [20].

3.4. Spatial discretisation

The standard approach to implementing an MHD exenterate, within the staggered variable arrangement, as used in the base flow solver presented earlier, would be to collocate the Lorentz force with the velocity components at the faces of each cell. However, due to the cross products involved in the calculation of the Lorentz forces, calculating the force field at each location requires the gradients of the electric potential in the other two directions. In a similar fashion, the calculation of each current density component involves the velocities in the other two directions. The effect of the interpolation scheme and of variable location have been proved to have a significant impact on the stability of the numerical algorithm and the scheme's monotonicity. Leboucher [36] has clearly indicated the numerical instabilities and inaccuracies that can be generated in finite volume MHD simulations using an ordinary staggered grid discretisation. To preserve monotonicity, he proposed using a fully staggered grid, where the electric potential is defined at the edges of each computational cell. Switching to a fully staggered variable configuration, such as the one proposed by Leboucher [36], could indeed satisfy

the monotonicity of the numerical method and the conservative nature of current calculations. However, since in this scheme the electric potential is not collocated with the pressure, any existing cell-centered pressure solvers could not be directly used for the poisson solution of Φ. Consequently, a completely new poisson solver would have to be used. Apart from the extra programming effort, such a solver would probably not match the excellent characteristics of direct solvers in terms of robustness and efficiency.

Recently, Ni et al. [33] also examined the effect of variable location on the consistency and the conservative nature of the staggered algorithm. Using Taylor series expansions, they clearly demonstrated that the numerical instabilities observed by Leboucher are due to the leading error terms present in the calculation of the electric potential gradients on non-uniform grids. In response, they proposed a numerical scheme for a collocated grid system, which was found to be conservative and consistent for the calculation of MHD flows at high Hartmann numbers. While such a collocated approach is promising, switching from a staggered to a collocated grid arrangement for an MHD solver implies major code modifications. More significantly, staggering has been successfully used to avoid checkerboard phenomena in the pressure solution, a property that we would prefer to preserve.

Taking the above considerations into account, we propose a new numerical methodology that can be used in existing flow solvers that are based on a staggered flow configuration. The new scheme retains the prime variable location and uses the same poisson solver for both the pressure and electric potential solutions. In the approach we have adopted, the electrostatic potential Φ is collocated with the pressure p at the center of each cell. Several choices exist for the location of the remaining variables involved in MHD calculations (Fig. 2(a) and (b)). For that purpose, one can consider the decomposition of the current density vector field into three parts. The first part is the electric field $\vec{J}_{\Phi_i}$, the second is the cross product $\vec{J}_u$ and the last part corresponds to the IB forcing $\vec{f}_{j,IB}$, namely,

$$\vec{J} = \underbrace{-\nabla\Phi}_{\vec{J}_{\Phi_i}} + \underbrace{(\vec{u}\times\hat{b}_o)}_{\vec{J}_u} + \vec{f}_{j,IB}. \tag{22}$$

Two different variants of the location of the current density and the associated Lorentz forces F_{Li} have been considered and tested for the present study. These are discussed next.

3.4.1. Staggered variant a

In the first variant considered, all the variables related to MHD are defined in a staggered fashion as shown in Fig. 2(a). Since the electric potential Φ is collocated with the pressure location at the node center, the first term of Eq. (22) can be naturally computed at each face without any need for interpolation. Thus, in consistency with the pressure gradient involved in momentum equations, the components of $\vec{J}_{\Phi_i}$ can then be computed according to,

$$\begin{aligned}
\vec{J}_{\Phi_x}|_{i+1/2,j,k} &= -\frac{\Phi_{i+1}-\Phi_i}{x_{i+1}-x_i}\\
\vec{J}_{\Phi_y}|_{i,j+1/2,k} &= -\frac{\Phi_{j+1}-\Phi_j}{y_{j+1}-y_j}\\
\vec{J}_{\Phi_z}|_{i,j,k+1/2} &= -\frac{\Phi_{k+1}-\Phi_k}{z_{k+1}-z_k},
\end{aligned} \tag{23}$$

where i,j or k locations are implied when subscripts are omitted. The second part of current density $\vec{J}_u$ has to be computed from interpolated values of the primary variables, i.e.

$$\begin{aligned}
\vec{J}_u|_{i+1/2,j,k} &= (v|_{i+1/2}\,\hat{b}_{o,z}|_{i+1/2} - w|_{i+1/2}\,\hat{b}_{o,y}|_{i+1/2})\\
\vec{J}_v|_{i,j+1/2,k} &= (w|_{j+1/2}\,\hat{b}_{o,x}|_{j+1/2} - u|_{j+1/2}\,\hat{b}_{o,z}|_{j+1/2})\\
\vec{J}_w|_{i,j,k+1/2} &= (u|_{k+1/2}\,\hat{b}_{o,y}|_{k+1/2} - v|_{k+1/2}\,\hat{b}_{o,x}|_{k+1/2}),
\end{aligned} \tag{24}$$

where the consistent interpolation proposed by Ni et al. [33] was used to transfer the properties to the face needed. As far as the IB forcing terms $\vec{f}_{j,IB}$ for the current density are concerned, these have to be imposed on a staggered fashion also, i.e. separately

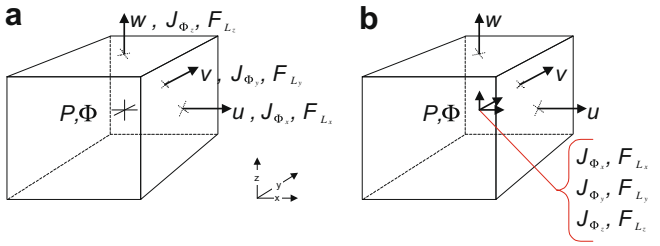

Fig. 2. Definition of variable location involved in MHD calculations, (a) variant *a* with ordinary staggered locations and (b) variant *b* with collocated variable arrangement.

for each component, as explained in Section 3.3. In the present variant, calculating the sources of the poisson equation for the electric potential of the provisional current density field J^* from Eq. (17) does not require any interpolation. Finally, the Lorentz forces can then be computed from,

$$\begin{aligned}
\vec{F}_{Lx}|_{i+1/2,j,k} &= (J_y|_{i+1/2}\,\hat{b}_{o,z}|_{i+1/2} - J_z|_{i+1/2}\,\hat{b}_{o,y}|_{i+1/2}) \\
\vec{F}_{Ly}|_{i,j+1/2,k} &= (J_z|_{j+1/2}\,\hat{b}_{o,x}|_{j+1/2} - J_x|_{j+1/2}\,\hat{b}_{o,z}|_{j+1/2}) \\
\vec{F}_{Lz}|_{i,j,k+1/2} &= (J_x|_{k+1/2}\,\hat{b}_{o,y}|_{k+1/2} - J_y|_{k+1/2}\,\hat{b}_{o,x}|_{k+1/2}).
\end{aligned} \tag{25}$$

using the same interpolation scheme as in the case of velocities.

3.4.2. Cell-centered variant b

In the second variant, all the variables related to MHD are defined in a cell-centered fashion. The current density due to the electric field is then computed based on a cell-centered electric potential using,

$$\begin{aligned}
\vec{J}_{\Phi_x}|_{i,j,k} &= -\frac{1}{2}\left[\frac{\Phi_{i+1}-\Phi_i}{x_{i+1}-x_i} + \frac{\Phi_i-\Phi_{i-1}}{x_i-x_{i-1}}\right] \\
\vec{J}_{\Phi_y}|_{i,j,k} &= -\frac{1}{2}\left[\frac{\Phi_{j+1}-\Phi_j}{y_{j+1}-y_j} + \frac{\Phi_j-\Phi_{j-1}}{y_j-y_{j-1}}\right] \\
\vec{J}_{\Phi_z}|_{i,j,k} &= -\frac{1}{2}\left[\frac{\Phi_{k+1}-\Phi_k}{z_{k+1}-z_k} + \frac{\Phi_k-\Phi_{k-1}}{z_k-z_{k-1}}\right].
\end{aligned} \tag{26}$$

The second part of current density $\vec{J}_u$ is computed from the interpolated velocity values at the cell-centers $u_{ci} = 1/2(u_{i+1/2} + u_{i-1/2})$ using,

$$\begin{aligned}
\vec{J}_u|_{i,j,k} &= (v_c|_i\,\hat{b}_{o,z}|_i - w_c|_i\,\hat{b}_{o,y}|_i) \\
\vec{J}_v|_{i,j,k} &= (w_c|_j\,\hat{b}_{o,x}|_j - u_c|_j\,\hat{b}_{o,z}|_j) \\
\vec{J}_w|_{i,j,k} &= (u_c|_k\,\hat{b}_{o,y}|_k - v_c|_k\,\hat{b}_{o,x}|_k).
\end{aligned} \tag{27}$$

The IB forcing terms $\vec{f}_{j,IB}$ can be calculated for all components in a cell-centered fashion, as explained in Section 3.3. A linear interpolation of the assembled current density is needed in order to compute the sources for the electric potential of the provisional current density field J^* according to Eq. (17). The Lorentz forces can then be computed using

$$\begin{aligned}
\vec{F}_{Lx}|_{i,j,k} &= (J_y|_i\,\hat{b}_{o,z}|_i - J_z|_i\,\hat{b}_{o,y}|_i) \\
\vec{F}_{Ly}|_{i,j,k} &= (J_z|_j\,\hat{b}_{o,x}|_j - J_x|_j\,\hat{b}_{o,z}|_j) \\
\vec{F}_{Lz}|_{i,j,k} &= (J_x|_k\,\hat{b}_{o,y}|_k - J_y|_k\,\hat{b}_{o,x}|_k).
\end{aligned} \tag{28}$$

When compared with the previous variant, one can clearly see that fewer interpolation operations are involved, namely one for the electric potential source and one for the transfer of Lorentz forces at the cell faces before adding them to the momentum equations.

3.5. Computational cycle

The time-advancement scheme adopted for the numerical solution of the present MHD case consists of the following computational cycle:

(1) Using the known velocity field at time level n and the electric potential $\Phi|^{n-1}$, the provisional current density $\vec{J}^*$ field is computed (Eq. (15)).
(2) Forcing is applied for the provisional current field according to the boundary conditions along the immersed surfaces (Eq. (14)).
(3) Poisson equation (Eq. (17)) is solved for the electric potential difference using the forced provisional current density field $\vec{J}^*$.
(4) The current density field (Eq. (18)) is projected according to the computed electric potential correction (Eq. (19)), so that the charge conservation law $\nabla \cdot \vec{J} = 0$ is satisfied.
(5) The forcing for the current field is reapplied according to the boundary conditions along the immersed surfaces (Eq. (14)).
(6) Lorentz force terms $N(J \times \hat{b}_o)$ are assembled using Eqs. (25) or (28) depending on the scheme used.
(7) Pressure, viscous, IB forces, and the computed Lorentz force, are all introduced as a source term in the momentum Eq. (7), and the provisional velocity field $\vec{u}^*$ at the next time step is estimated.

(8) Using the mass residual of the provisional velocity field $\vec{u}^*$, a Poisson equation for pressure correction is solved (Eq. (8)).
(9) The velocities and pressures are projected to the incompressible space by applying the pressure correction (Eqs. (9) and (10)) so that mass continuity is also satisfied.

It should be noted, that step (5) could be omitted if the Lorentz forces are computed from $N[(-\nabla\Phi + \vec{u}_i \times \hat{b}_o) \times \hat{b}_o]$, but in that case the final current density field at time level n would not comply with the applied electromagnetic boundary conditions along the immersed interfaces.

Within the quasi-static approach adopted here, a variable time step is used for the calculations, which is dynamically adjusted according to the convective (CFL) and viscous time scale (VSL) criteria: CFL < 0.2 and VSL < 0.05. Due to the efficiency of the direct poisson solvers used, the resulting computer code has excellent parallel efficiency and requires a limited amount of physical memory (135 Mb per million nodes). For a fully 3D hydrodynamic calculation performances of 0.28 μs/node/cycle were reached and for a full MHD problem with a space varying magnetic field, 0.52 μs/node/cycle (on Dual AMD@2.6 GHz processors). Thus, the computational overhead associated with the MHD solution (solving the poisson equation, computing currents with IB method, including forces, etc.) was of the order of 80%.

4. Results

4.1. Decaying vortex case

In the numerical procedure presented in the previous sections, the charge conservation law is imposed and satisfied by a projection scheme and an electrostatic potential correction equation. The fundamental importance of the charge conservation law motivated the close examination of the accuracy that the present method can achieve. For that purpose, it was chosen to first investigate the spatial and temporal accuracy properties of the method in a simple, well-posed MHD problem in the absence of solid boundaries. In hydrodynamic simulations, similar accuracy tests usually consider the unsteady problem of a decaying vortex [32,37] described by,

$$\begin{aligned} u(x,z) &= -\cos(x)\,\sin(z)\,e^{-2t} \\ w(x,z) &= \sin(x)\,\cos(z)\,e^{-2t} \\ p(x,z) &= -\frac{1}{4}[\cos(2x)+\cos(2z)]\,e^{-4t}, \end{aligned} \tag{29}$$

where $(x,z) \in [0,\pi]$. Eq. (29) satisfy continuity and form an exact solution of the N–S equations. In MHD simulations, an equivalently elegant unsteady problem with an exact analytical solution has not been posed and utilised in previously conducted studies. For these reasons, we considered the above mentioned flow problem by imposing a uniform field $\hat{b}_{o,y}$ along y direction, normally to the plane of vortex motion. In such a configuration, one can easily show that the solenoidal condition of the current density field leads to the following equation for electrostatic potential,

$$\nabla^2\Phi = -2\,\hat{b}_{o,y}\,\cos(x)\,\cos(z)\,e^{-2t}, \tag{30}$$

which has a simple family of solutions in the form,

$$\Phi = \hat{b}_{o,y}\,\cos(x)\,\cos(z)\,e^{-2t} + C = -\frac{\hat{b}_{o,y}\omega_y}{2} + C, \tag{31}$$

where C is an arbitrarily chosen additive constant. Under these conditions, the actual current density field as well as the Lorentz forces are naturally eliminated. One can thus validate the basic elements of a numerical methodology by solving such a problem and examining the time evolution of the generated electric potential and the velocity field, which should remain unaffected under the action of the magnetic field. Hence, a successful numerical test for such a MHD flow configuration should reproduce in the discrete sense: (i) an identical evolution of the velocity field with the hydrodynamic case according to Eq. (29), (ii) a non-zero electric potential according to Eq. (31), (iii) zero current density and Lorentz force fields.

That test was conducted in the present study by performing a series of two-dimensional simulations at various numerical resolutions using a staggered variable arrangement for the current density field (Section 3.4.1). Five different uniform grids were tested with 16^2, 32^2, 64^2, 128^2 and 256^2 cells. All simulations were performed at the same CFL number so that a linear relationship was established between the spatial step size Δx and the temporal step size Δt.

Fig. 3 presents the time evolution of the L_2 norms of maximum errors for a total time of 2 characteristic time units d/u_{max}. As the mesh is refined, the method preserves a second order accuracy for both the velocity field and the electric potential. These tests provide an evidence of the capability of the computational cycle presented in section 3.5 to satisfy both the mass and the charge conservation laws. Additionally, the current density projection scheme consisting of Eqs. (17)–(19) seems

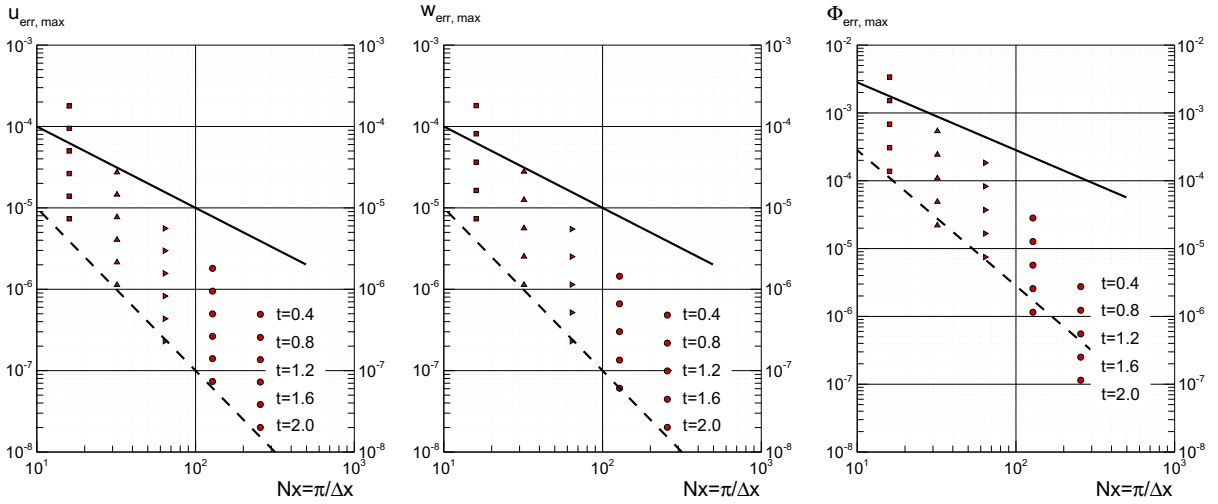

Fig. 3. MHD flow in a decaying vortex with a magnetic field applied along the spanwise direction y. Effect of numerical resolution on the time evolution of the maximum error with respect to the analytical solution. Maximum error in streamwise velocity u/u_{max} (left), transverse velocity w/w_{max} (middle) and electric potential Φ (right). Solid and dashed lines correspond to slopes of -1 and -2, respectively.

capable to accurately follow the evolution of in unsteady cases with a second order spatial and temporal accuracy. The same conclusion is drawn from similar tests that were performed for wall-bounded MHD flows, presented in the next sections.

4.2. Hartmann duct flow at $Ha = 500 - 2000$

In order to validate and verify the algorithmic consistency of the proposed projection scheme for the current density and the electric potential correction in the presence of solid boundaries, a series of fully-developed channel and duct flows were considered. These tests also allowed the performance investigation of the two different discretisation methods presented in Section 3.4.1 and 3.4.2 with respect to the variable location. Since these preliminary calculations were conducted in order to test the fundamental elements of the proposed methodology, for simplicity and clarity reasons these simulations did not use the IB methodology or a forcing scheme for current density (which are validated in Sections 4.3 and 4.4).

A Hartmann duct flow was considered with the flow aligned along the x direction, in a duct of cross section $2d \times 2d$ in y- and z-directions. Using the maximum velocity u_{max} in the duct as a characteristic velocity, the Reynolds number was fixed at $Re = \frac{u_{max} d}{\nu} = 100$, while the Hartmann number considered was in the range $Ha = 500 - 2000$. All solid walls were assumed insulating, and a uniform magnetic field was applied along the z-direction.

Periodic boundary conditions have been used along the streamwise direction, and a forcing term was supplied to the momentum equations, so that a constant flow rate was maintained during the simulation. A relatively coarse grid of $4 \times 64 \times 64$ cells was used with uniform grid spacing in x-direction. The same, linearly expanding grid was used along y- and z-directions with a minimum grid spacing of $\Delta z_{min} = \Delta y_{min} = 0.005d$, so that the Hartmann layers of thickness $1/Ha$ were fully resolved.

Fig. 4(a) a presents the simulation results for the ordinary staggered variable arrangement (variant a of Section 3.4.1). The resolution of the Hartmann and side layers was very accurately captured for this variant, and the solution did not suffer from any kind of numerical instabilities. Even with a coarse numerical resolution, and a very high linear expansion ratio of $1.1 - 1.2$ for the grid spacing, a fully consistent and conservative solution was obtained. The solution did not suffer from numerical instabilities as those reported in [36] for staggered variable arrangement. This is mainly due to the interpolation used to transfer the properties to the face needed after Ni et al. [33]. They demonstrated that their consistent interpolation scheme can ensure divergence-free current densities and guarantee the conservative properties of the computed solutions.

In contrast, when using a collocated variable definition (variant b of Section 3.4.2), spurious oscillations were apparent, and numerical instabilities were generated at the very first calculation steps. As shown in Fig. 4(b), current density circulations were significantly distorted close to the side layers. These numerical instabilities are similar to the ones found in [36], and could be therefore assigned to the inclusion of the $u \times B$ term to the current density field. Introducing the idea proposed by Leboucher [36] (which was originally developed for a cell-centered definition of flow variables), did not stabilise the solution or improve the simulation results of variant b.

Therefore, the scheme based on a staggered variable definition (variant a of Section 3.4.1) was selected as more appropriate for consistent MHD simulations presented in the present study. Extensive tests on Hartmann flows with or without side walls at various Ha numbers verified the consistency of that scheme. Fig. 5 shows numerical predictions for the Hartmann and side

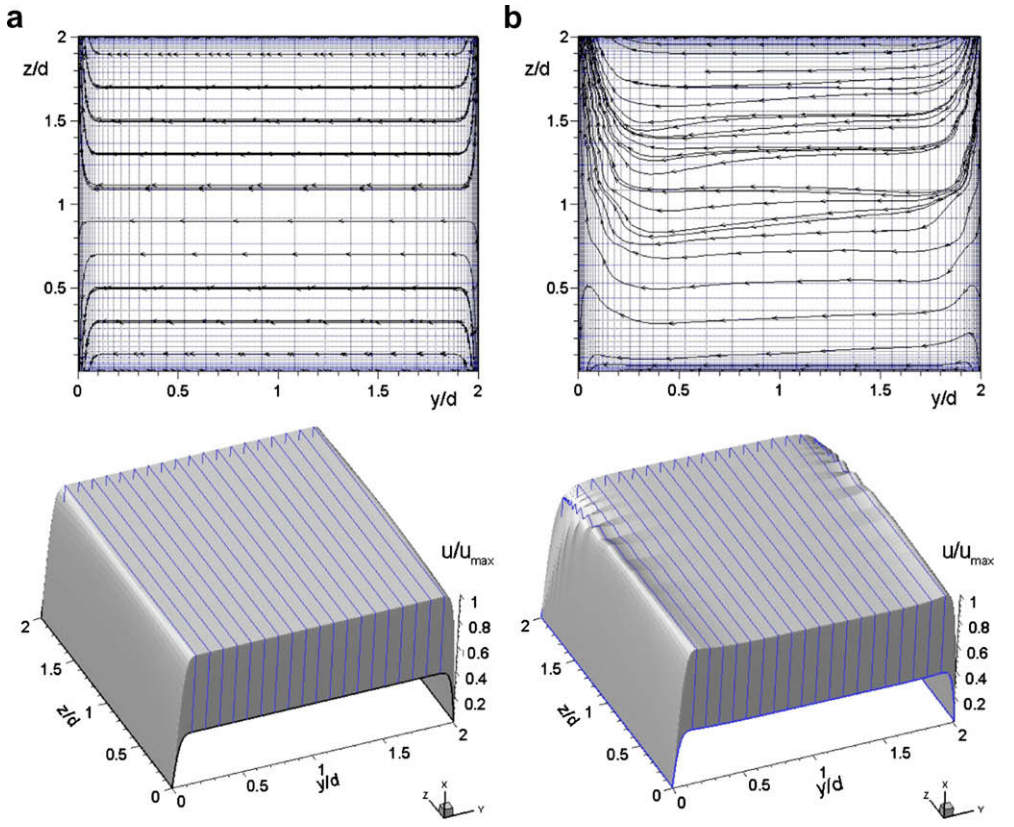

Fig. 4. Predicted current density field and numerical grid (top) and velocity (bottom) for a Hartmann duct flow at $Ha = 2000$ using different discretisation methods and a numerical grid of $4 \times 64 \times 64$ cells. (a) Face centered, ordinary staggered definition of MHD variables [variant *a*, Section 3.4.1], (b) collocated definition of variables [variant *b*, Section 3.4.2].

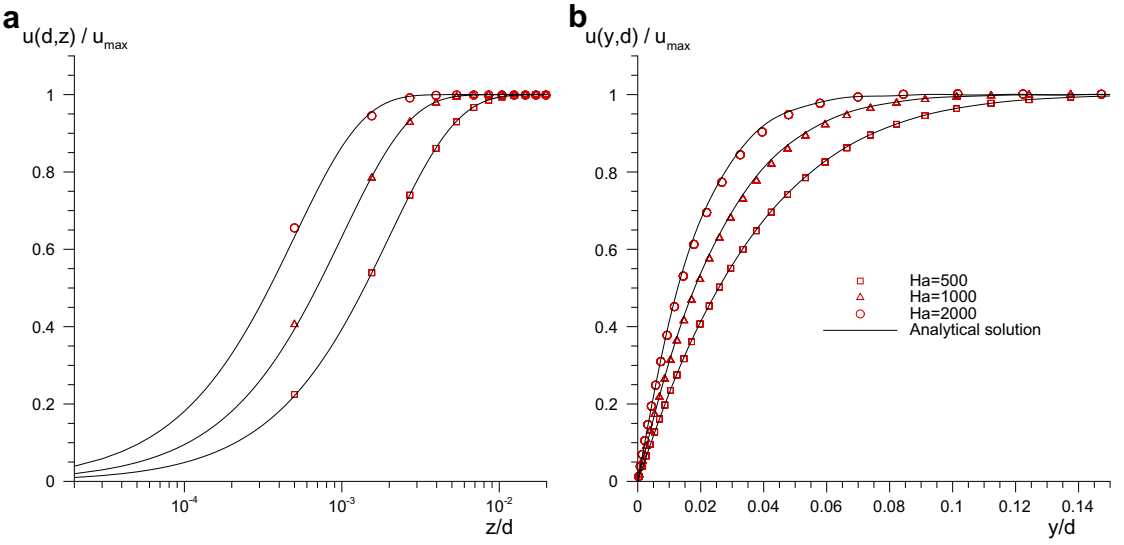

Fig. 5. Hartmann and side layers for a fully-developed duct flow at various *Ha* numbers with insulating solid walls (Schercliff case). Comparisons with analytical solutions for the (a) Hartmann layers and (b) side layers, using a coarse grid of 98×98 cells.

walls against analytical solutions for $Ha = 500 - 2000$. For all examined cases, the agreement was exceptional even when relatively coarse numerical resolutions were used.

4.3. MHD flow in a diverting channel at Ha=20,100

Once the basic algorithmic procedure was verified, a series of simulations using the proposed IB method were conducted. For that purpose, the flow in a two-dimensional diverting channel was examined with the geometrical definition shown in Fig. 6. Two opposite-facing blunt plates of thickness $0.5d$ were introduced inside a plane channel of length $10d$ and width $2.5d$ to create a flow diversion at location $x = 2d$. Solid surfaces were prescribed using the IB method as a series of line segments and circular arcs and the forcing procedure presented in Section 3.3 was used.

Once the flow recovers after the diversion, it should resemble and actually match the characteristics of a Hartmann or a side layer (depending on the direction of the applied magnetic field), where analytical solutions exist. Two different magnetic field directions were considered, a spanwise magnetic field at $Ha = 100$, and a wall-normal magnetic field at $Ha = 20$, with Stuart numbers $N = 1000$ and $N = 40$, respectively. Therefore, a relatively long domain of $10d$ and a low Reynolds number $Re = 10$ (based on the maximum velocity u_{max}) were selected in order to minimise the effect of any recirculation region and provide sufficient space for flow recovery at the exit of the domain.

A uniform inlet velocity profile was imposed at the inlet for all cases, and convective boundary conditions were applied at the domain's outlet [38]. In order to examine the accuracy of the proposed IB methodology and grid resolution effects, three different uniform grids were used as shown in Table 1. All simulations were performed at the same CFL number and for the same total time, so that a detailed error analysis with respect to the spatial and temporal order of accuracy could be conducted. A total time of 40 characteristic time units d/u_{max} was proved to be sufficient to reach steady state conditions.

For the case of a spanwise magnetic field, an electric potential is generated and side layers are formed along the solid surfaces. The flow close to the domain's outlet is then expected to match exactly the case of a plane channel at identical MHD conditions. Due to the spanwise orientation of the magnetic field, the velocity field should remain unaffected by the existence of the magnetic field in regions where the streamlines are parallel to x-direction. Thus, provided that a sufficient

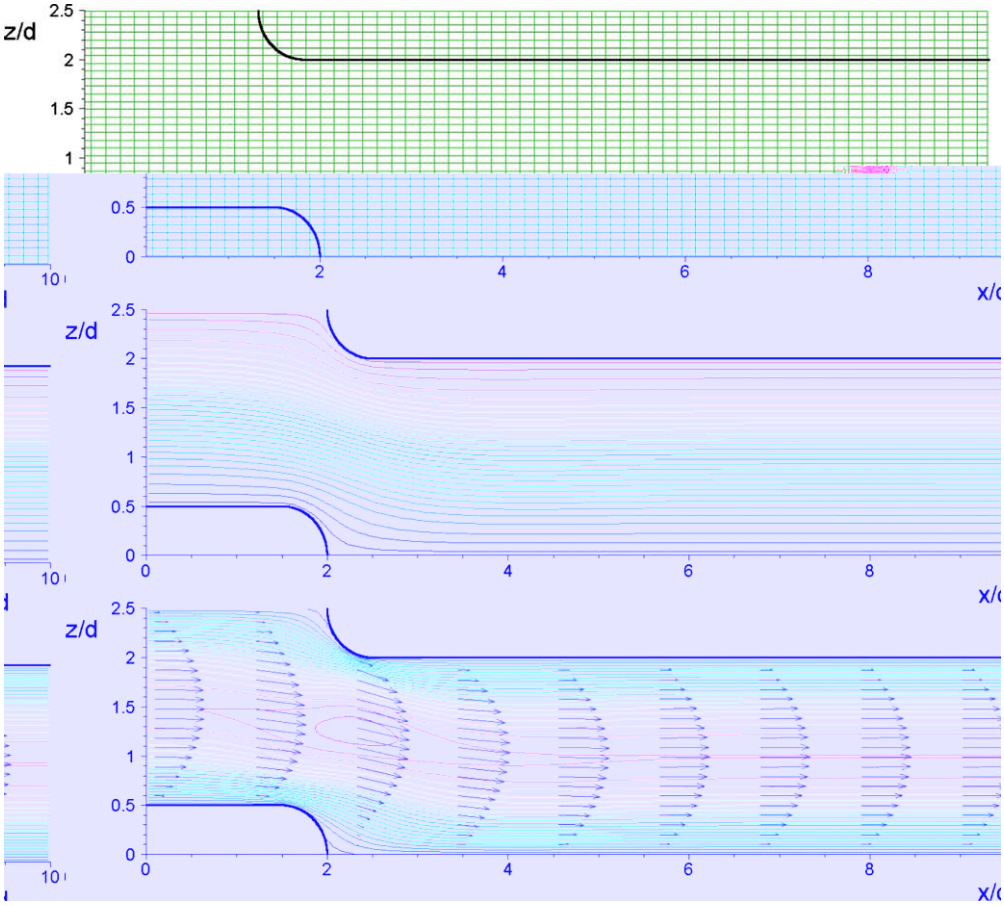

Fig. 6. MHD simulation of a diverting channel with immersed boundaries at $Ha = 100$ with a spanwise applied magnetic field, (upper): geometrical configuration and computational grid Gd2 (every fourth point shown), (middle): predicted distribution of electric potential, (bottom) velocity vector field and contour lines of streamwise velocity component.

Table 1
Numerical grids used for MHD simulations in a diverting channel.

Grid	$Nx \times Nz$	Δ_x/d, Δ_z/d
Gd1	128×64	0.0781250, 0.0390625
Gd2	256×128	0.0390625, 0.0195312
Gd3	512×256	0.0195312, 0.0097656

recovery length is included, the solution along the outlet of the domain should exactly match a parabolic distribution. The same time, the electric potential should vary in the range $-d < z < d$, according to,

$$\Phi(z) = \frac{-\hat{b}_{o,y}\, d^2}{\nu\rho}\frac{\Delta p}{\Delta x}\left(1 - \frac{z^2}{3d^2}\right), \tag{32}$$

where $\hat{b}_{o,y}$ is the intensity of the magnetic field along y-direction and $\frac{\Delta p}{\Delta x}$ is the mean pressure gradient driving the flow.

That is demonstrated in Figs. 6 and 7(a), where a clearly parabolic velocity profile was predicted close to the inlet and along the outlet of the domain. The distribution of electric potential and the spanwise vorticity ω_y shown in Fig. 7(b), clearly demonstrates the validity of the applied forcing scheme. The proper variation of electric potential and spanwise vorticity close to solid surfaces are recovered at both sections, while $d\Phi/dn$ clearly vanishes close to the immersed surface, eliminating wall-normal currents.

The three different numerical resolutions produced almost indistinguishable results for the properties of interest. A detailed analysis of the error associated with each grid resolution is presented in Fig. 8. The variation of the L_2 norm of the velocity, electric potential and vorticity clearly indicates the retainment of a second order of accuracy in space and time.

When a magnetic field is applied along the z-direction, the electric potential is not generated and the electric field is absent. However, due to the orientation of the magnetic field, the spanwise component of the current density J_y is present due to the $u \times B$ term, leading to the activation of Lorentz forces and the formation of Hartmann layers.

Fig. 9 shows the predicted distribution of velocity, current density, Lorentz force and vorticity in the vicinity of the immersed wall-surfaces. An excellent agreement with respect to the analytical solution is found for all quantities, even for the coarser grid Gd1, despite the marginal resolution of the Hartmann layers with $\Delta z = 0.078d$. Hartmann layers are accurately captured in all cases, indicating the potential of the proposed IB method to represent immersed surfaces.

The error analysis performed for this case, leads to the same conclusion with respect to the spatial and temporal accuracy of the scheme. Fig. 10 presents the computed L_2 norm of the error in velocity, current density and Lorentz force. As in the previous reported case, the method preserves at least second order of accuracy for all the associated variables.

4.4. 3D magnetohydrodynamic case

In order to fully verify the accuracy and the potential of the present IB method, the three-dimensional unsteady flow around a circular cylinder was also studied. For laminar, purely two-dimensional flows around an unconfined cylinder the electric field is absent and does not contribute to the computed current density $\vec{J}$ for an aligned or a transverse direction

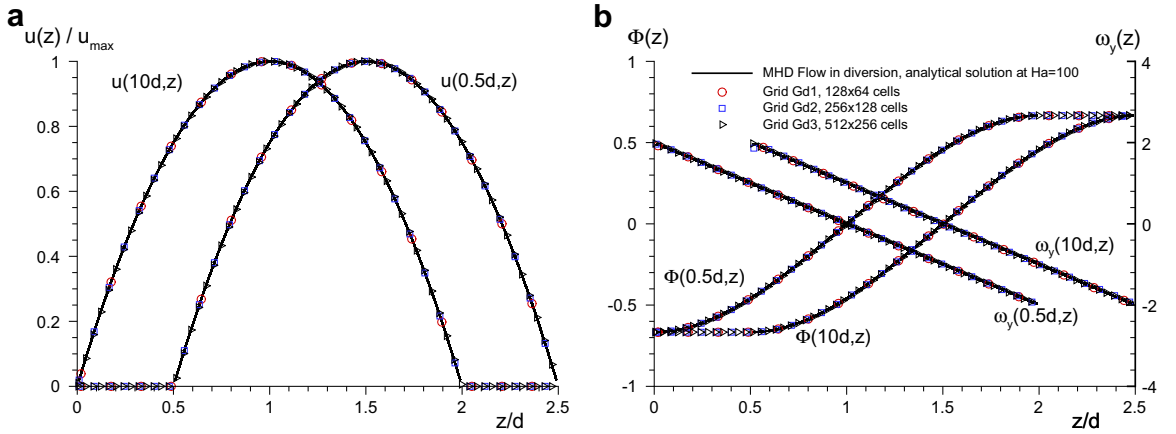

Fig. 7. MHD flow in a diverting channel with a magnetic field applied along the spanwise direction y. Comparison at the inlet ($x/d = 0.5$) and outlet ($x/d = 10d$) sections against the analytical solution at $Ha = 100$: (a) velocity profile $u(z)$, (b) electric potential $\Phi(z)$ and spanwise vorticity distribution ω_y (every fourth point shown).

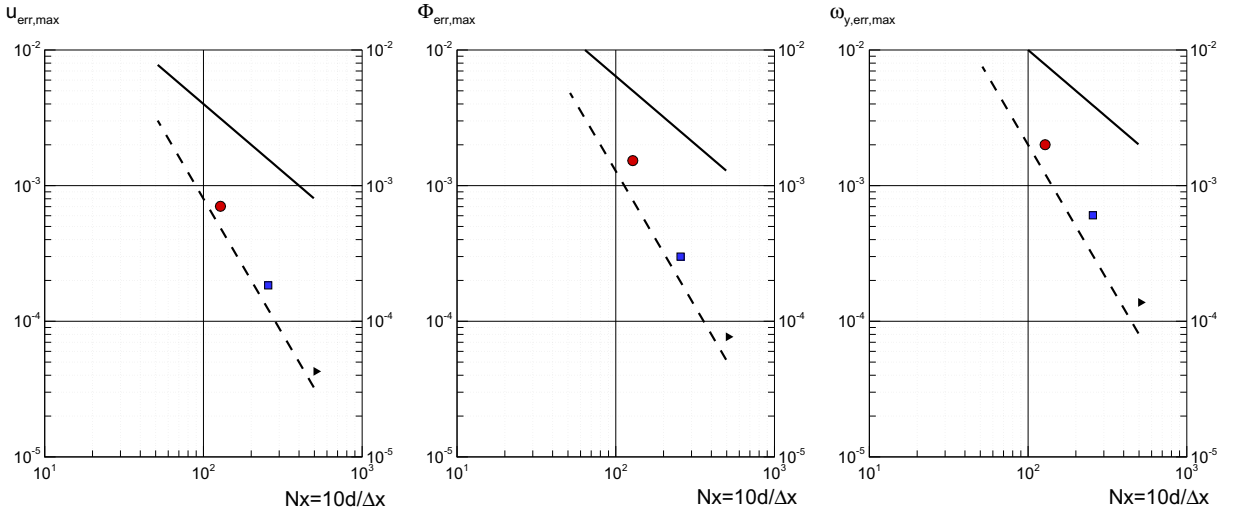

Fig. 8. MHD flow in a diverting channel with a magnetic field applied along the spanwise direction. Effect of numerical resolution on the maximum error with respect to the analytical solution at the outlet of the domain. Maximum error in velocity u/u_{max} (left), electric potential Φ (middle), spanwise vorticity ω_y (right). (circle): Gd1, (square): Gd2, (triangle): Gd3, solid and dashed lines correspond to slopes of -1 and -2, respectively.

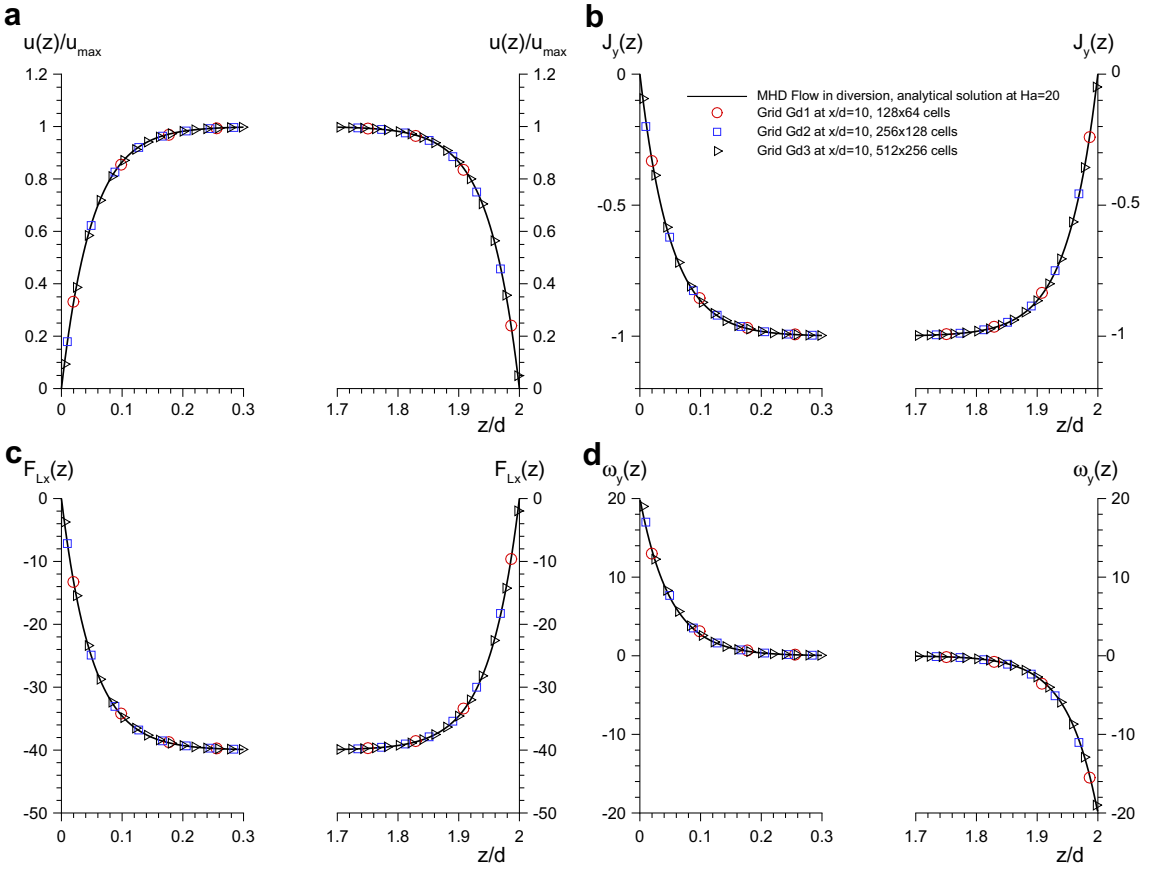

Fig. 9. Formation of Hartmann layers for the MHD flow in a diverting channel with a magnetic field applied along the wall-normal direction z. Comparison along the outlet of the domain ($x/d = 10d$) against the analytical solution at $Ha = 20$: (a) velocity profile $u(z)$, (b) current density $J_y(z)$, (c) streamwise component of the Lorentz force F_{Lx} and (d) spanwise vorticity ω_y distribution (every second point shown, the region $0.3d < z < 1.7d$ is omitted to focus on the Hartmann layers).

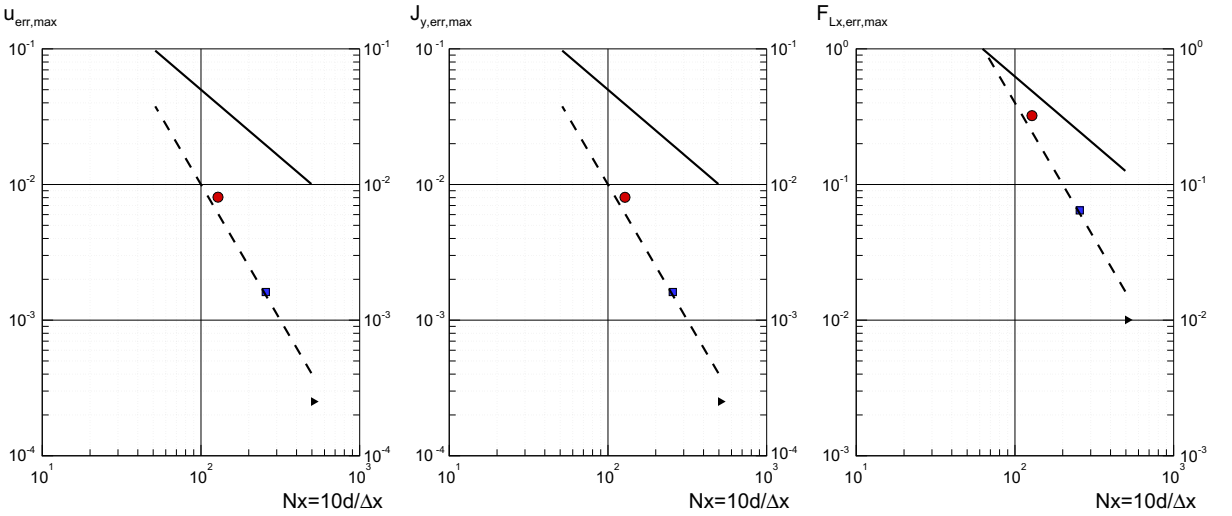

Fig. 10. MHD flow in a diverting channel with a magnetic field applied along z direction. Effect of numerical resolution on the maximum error with respect to the analytical solution at the outlet of the domain. Maximum error in: velocity u/u_{max} (left), current density $J_y(z)$ (middle), streamwise component of the Lorentz force F_{Lx} (right). (circle): Gd1, (square): Gd2, (triangle): Gd3, solid and dashed lines correspond to slopes of -1 and -2, respectively.

of the magnetic field. For Reynolds numbers $Re > 194$ though, the flow becomes three-dimensional and mode-A instability occurs [39,40]. Under these conditions, the application of a magnetic field aligned with the flow would activate the electric field since the electric potential Φ is driven by the source term ω_x for an aligned magnetic field (Eq. (12)). Therefore, the three-dimensional case at $Re_d = 200$ was also computed in order to validate the IB methodology for the estimation of the electric field $\vec{E}$. The results of these 3D simulations are compared against previously reported data from Mutschke et al. [41] for a streamwise applied field at $N = 0, 0.2, 1$.

A non-conducting circular cylinder of diameter d was described with the IB methodology presented at a distance of $L_i = 7d$ from the domain's inlet and the outlet is located at $L_o = 12d$ behind the body. In the vertical direction z, the cylinder is symmetrically placed along the centerline with the domain extending to $L_z = 15d$. Along the surface of the immersed cylinder, non-slip wall boundary conditions were used. At the domain's inlet, a constant velocity profile is imposed, while convective outflow conditions have been specified for the outlet. Along the z direction, Neumann and Dirichlet boundary conditions have been applied for the streamwise and transverse velocity components u and w, respectively, i.e.

$$\left.\frac{\partial u}{\partial z}\right|_{z=0,L_z} = 0 \quad \text{and} \quad w|_{z=0,L_z} = 0. \tag{33}$$

Two different grids have been used, a coarse grid Gc1, with $113 \times 32 \times 96$ cells and a finer one Gc2 with $262 \times 64 \times 192$ cells. The first grid uses 20×20 and the second 40×40 cells to resolve the area $d \times d$ around the cylinder. Linear grid stretching has been applied for both grids along the streamwise and transverse direction, and uniform grid along the spanwise direction. Two different Hartman numbers have been considered, namely $Ha = 6.32$, and $Ha = 14.14$ with $Nx = 0.2$ and $N_x = 1.0$, respectively.

All simulations started from the purely hydrodynamic field which was first computed. Starting from a steady flow, the calculation evolved to a clearly 3D one as indicated by the formation of the vortex pairs due to the deformation of the primary vortices in the cylinder's wake. The wavelength of these structures was found to be $\lambda \approx 3.4d$, in agreement with previous studies [40]. For the lower Hartmann number case considered, the flow remains unstable, and a reduction in the computed value of the drag coefficient $\overline{C_d}$ is noticed with respect to the purely hydrodynamic case. In the higher Hartmann number case, the values of drag coefficient increase above the hydrodynamic value and the flow initially returns to two-dimensionality. In later times, due to the action of the Lorentz forces, the flow becomes completely stabilised and vortex shedding is diminished.

This is demonstrated in Fig. 11 which presents the instantaneous patterns for the higher Hartmann number case shortly after the application of the magnetic field and before the return to two-dimensionality. As shown in a variety of previous two-dimensional studies for that MHD flow, a narrower wake is produced by the action of the Lorentz forces as shown in Figs. 11(a), (b), and (d).

As previously mentioned the existence of streamwise vorticity ω_x (Fig. 11(c)) acts as a source term to the electrostatic potential (Fig. 11(e)). As a result the current density (Fig. 11(f)) is activated and the Lorentz forces eventually eliminate the instability by opposing and suppressing vorticity.

Table 2 summarises the cases presented here and the computed coefficients, including the comparison for the hydrodynamic case at $N = 0$. The critical Stuart number for the transition to a purely 2D also flow was found to take place for interaction

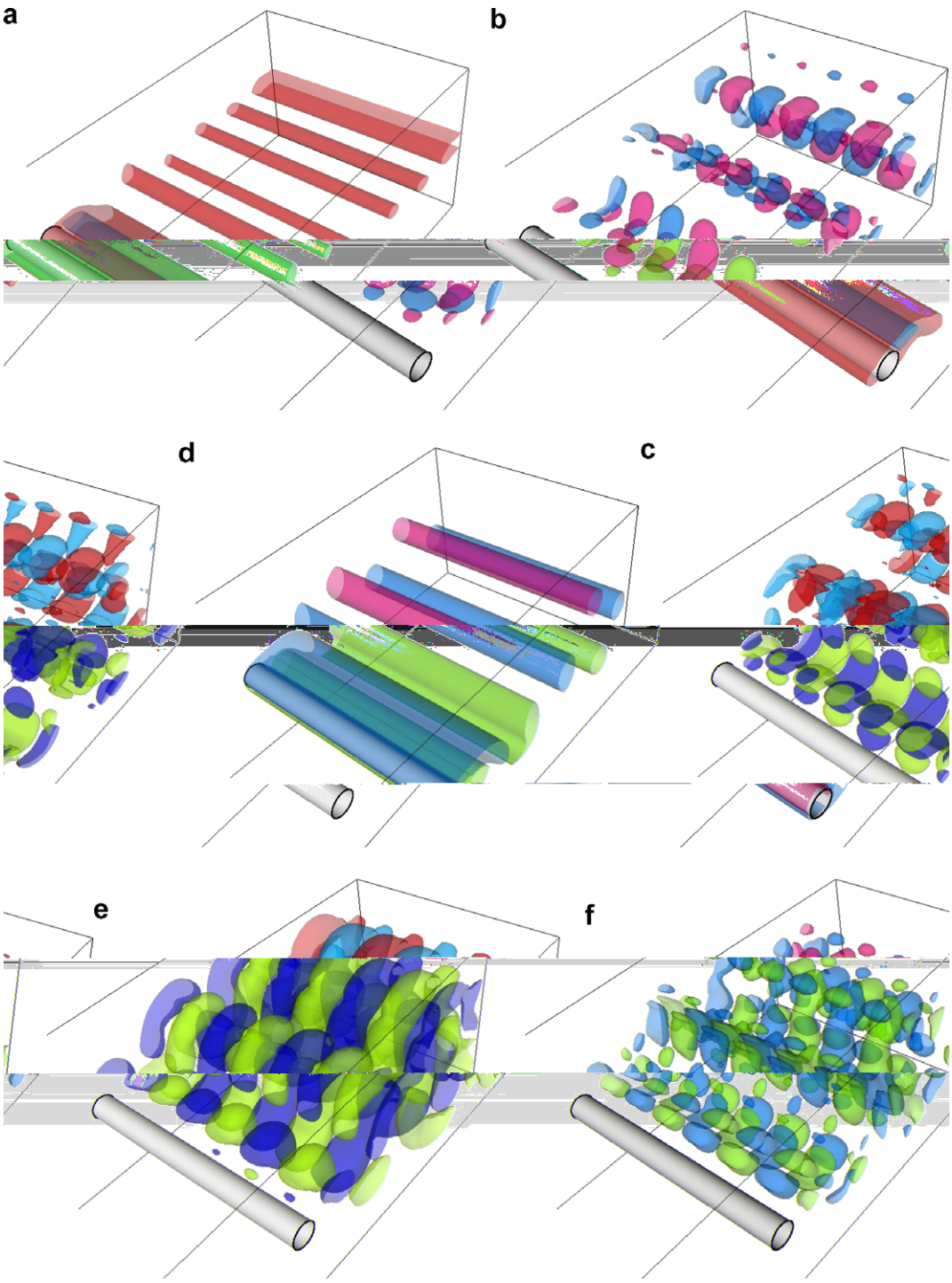

Fig. 11. Instantaneous patterns at $Re_d = 200$, with $N_x = 0.4$ using grid Gc2. Dark and light surfaces correspond to positive and negative values, (a) streamwise velocity $u = -0.05, 0.6$, (b) spanwise velocity $v = \pm 2 \times 10^{-5}$, (c) streamwise vorticity $\omega_x = \pm 5 \times 10^{-4}$, (d) spanwise vorticity $\omega_y = \pm 1$, (e) electric potential $\Phi = \pm 3 \times 10^{-5}$, and (f) streamwise current density $\vec{J}_x = \pm 3 \times 8^{-5}$.

parameter values $0.3 < N_x < 0.4$ as in the study of Mutschke et al. [41]. All predicted quantites were found in a very good agreement with previous studies for both numerical resolutions used. These global characteristics provide strong evidences about the accuracy of the proposed IB method, since they are closely related to the space and time variation of the forces exerted on the immersed cylinder.

Table 2
Predicted values of lift, drag coefficients, length of the recirculation region X_r and St numbers for the three-dimensional hydrodynamic ($N = 0$) and MHD flow around a circular cylinder at $Re_d = 200$.

Case (grid)	N_x	$\overline{C_d}$	C_l'	X_r	St
Present (Gc1)	0	1.29	0.50	0.97	0.204
Present (Gc2)	0	1.30	0.63	0.87	0.204
Zhang et al. [40]	0	1.29	0.53	–	0.201
Mutschke et al. [41]	0	1.30	0.60	–	0.197
Present (Gc1)	0.2	1.04	0.07	2.42	0.174
Present (Gc2)	0.2	1.08	0.09	2.23	0.172
Mutschke et al. [41]	0.2	1.07	0.09	–	–
Present (Gc1)	1.0	1.17	0.0	3.13	–
Present (Gc2)	1.0	1.20	0.0	3.10	–
Mutschke et al. [41]	1.0	1.19	0.0	3.11	–

5. Conclusions

The objective of the present study was to investigate the extension of the IB method for wall-bounded MHD simulations of liquid metals, which are of fundamental importance and are associated with high computational cost. A fully explicit projection scheme for current densities has been proposed using an electric potential correction. A forcing scheme was presented to simulate the location of arbitrary shaped non-conducting immersed surfaces inside the domain. The presented computational methodology can be easily implemented to extend the applicability of existing cartesian flow solvers that use a staggered variable arrangement.

Two different discretisation schemes were tested for the arrangement of the Lorentz forces and current densities. The cell-centered formulation was found to suffer from severe numerical instabilities, while ordinary staggering of current densities and Lorentz forces was proved to form a consistent variable arrangement with the flow solver used. In both cases, the electric potential was collocated with pressure so that the identical efficient direct solver was used for both variables in order to avoid computational complexity. The combined application of fast direct pressure solution and the IB method for the representation of complicated geometries was found to highly enhance computational efficiency, a crucial consideration for the computation of wall-bounded MHD flows.

Several steady and unsteady fully-developed and space-developing test cases were examined to validate the numerical methodology. All the examined cases were found to be in a very good agreement with existing analytical solutions and previously reported studied. Provided that the Hartmann and side layers are adequately resolved, the produced simulations have also indicated a very weak dependence on grid resolution. For all the test cases considered, the combined projection method and forcing scheme, as proposed herein, were found to recover the proper near-wall behavior for the current density field and the electric potential, while satisfying the charge conservation law in arbitrary shaped immersed surfaces.

From all the computed cases, it can be concluded that the proposed extension of the IB method can provide a valuable numerical tool for efficient and accurate three-dimensional simulations of wall-bounded MHD flows with arbitrarily shaped non-conducting surfaces. The extension of the method to MHD flows with conducting walls is under development.

Acknowledgment

E. Balaras is gratefully acknowledged for providing help on the implementation details of the IB method. This work has been performed under the UCY-CompSci project, a Marie Curie Transfer of Knowledge (TOK-DEV) grant (Contract No. MTKD-CT-2004-014199) funded by the CEC under the 6th Framework Program and the contract of association ERB 5005 CT 99 0100 between the European Atomic Energy Community and the Hellenic Republic. Partial support by a Center of Excellence grant from the Norwegian Research Council to Center for Biomedical Computing is also greatly acknowledged.

References

[1] N.B. Morley, S. Smolentsev, L. Barleon, I.R. Kirillov, M. Takahashi, Liquid Magnetohydrodynamics – recent progress and future direction for fusion, Fusion Eng. Design 51–52 (2000) 701–713.
[2] U. Müller, L. Bühler, Magnetohydrodynamics in Channels and Containers, Springer, 2001.
[3] R. Moreau, Magnetohydrodynamics, Kluwer, 1990.
[4] D.D. Papailiou, Magneto-fluid-mechanic turbulent vortex streets. In Fourth Beer-Sheva Seminar on MHD Flows and Turbulence, AIAA, 1984, pp. 152–173.
[5] Y. Kolesnikov, A. Tsinober, An experimental study of two-dimensional turbulence behind a grid, Fluid Dyn. 9 (1972) 621–624.
[6] J. Lahjomri, P. Caperan, A. Alemany, The cylinder wake in a magnetic field aligned with the velocity, J. Fluid Mech. 253 (1993) 421–448.
[7] B. Mück, C. Günther, U. Müller, L. Bühler, Three-dimensional MHD flows in rectangular ducts with internal obstacles, J. Fluid Mech. 418 (2000) 265–295.
[8] G. Mutschke, G. Gerbeth, V. Shatrov, A. Tomboulides, Two and three-dimensional instabilities of the cylinder wake in an aligned magnetic field, Phys. Fluids 9 (1997) 3114–3116.
[9] T.V.S. Sekhar, R. Sivakumar, H. Kumar, T.V.R. Ravi kumar, Effect of aligned magnetic field on the steady viscous flow past a circular cylinder, Appl. Math. Modell. 31 (2007) 130–139.

[10] G. Mutschke, V. Shatrov, G. Gerbeth, Cylinder wake control by magnetic fields in liquid metal flows, Exp. Thermal Fluid Sci. 16 (1998) 92–99.
[11] P. Moin, G. Iaccarino, Complex Effects in Large Eddy Simulations, in Complex effects in Large Eddy Simulations, in: Lecture Notes in Computational Science and Engineering 56, Springer, 2007.
[12] G. Kalitzin, J.A. Templeton, G. Medic, A Near-Wall Eddy-Viscosity Formulation for LES, in: Complex effects in Large Eddy Simulations, Lecture notes in computational Science and Engineering 56, Springer, 2007.
[13] A. Pothérat, J. Sommeria, R. Moreau, Effective boundary conditions for magnetohydrodynamic flows with thin Hartmann layers, Phys. Fluids 14 (1) (2002) 403–410.
[14] O. Widlund, Wall functions for numerical modeling of laminar MHD flows, Eur. J. Mech. B/Fluids 22 (2003) 221–237.
[15] C.S. Peskin, Flow patterns around heart valves: a numerical method, J. Comput. Phys. 10 (1972) 252–271.
[16] D. Goldstein, R. Handler, L. Sirovich, VDirect numerical simulation of turbulent flow over a modeled riblet covered surface, J. Fluid Mech. 302 (1995) 333–376.
[17] H.S. Udaykumar, R. Mittal, P. Rampunggoon, A. Khanna, A sharp interface Cartesian grid method for simulating flows with complex moving boundaries, J. Comput. Phys. 174 (2001) 345–380.
[18] Y.-H. Tseng, J.H. Ferziger, A ghost-cell immersed boundary method for flow in complex geometry, J. Comput. Phys. 192 (2003) 593–623.
[19] E.A. Fadlun, R. Verzicco, P. Orlandi, J. Mohd-Yusof, Combined immersed boundary finite-difference methods for three-dimensional complex simulations, J. Comput. Phys. 161 (2) (2000) 35–60.
[20] J. Yang, E. Balaras, An embedded-boundary formulation for large-eddy simulation of turbulent flows interacting with moving boundaries, J. Comput. Phys. 215 (1) (2006) 12–40.
[21] J. Kim, D. Kim, H. Choi, An immersed-boundary finite-volume method for simulations of flow in complex geometries, J. Comput. Phys. 171 (2001) 132–150.
[22] J. Mohd-Yusof, Development of immersed boundary methods for complex geometries. Annual Research Briefs 1998 325-336, Center Turbulence Res. 12 (1998) 1–2.
[23] D.G.E. Grigoriadis, J.G. Bartzis, A. Goulas, LES of the flow past a rectangular cylinder using the immersed boundary concept, Int. J. Num. Meth. Fluids 41 (2003) 615–632.
[24] M.C. Lai, C.S. Peskin, An immersed boundary method with formal second-order accuracy and reduced numerical viscosity, J. Comput. Phys. 160 (2000) 705–719.
[25] R. Verzicco, P. Orlandi, J. Mohd-Yusof, D. Haworth, LES in complex geometries using boundary body forces, AIAA J. 38 (2000) 427–433.
[26] E. Balaras, Modeling complex boundaries using an external force field on fixed Cartesian grids in large-eddy simulations, Comput. Fluids 33 (2004) 375–404.
[27] R. Mittal, G. Iaccarino, Immersed boundary methods, Annu. Rev. Fluid Mech. 37 (2005) 239–261.
[28] D.G.E. Grigoriadis, J.G. Bartzis, A. Goulas, Efficient treatment of complex geometries for large-eddy simulations of turbulent flows, Comput. Fluids 33 (2004) 201–222.
[29] U. Schumann, A direct method for the solution of Poisson's equation with Neumann boundary conditions on a staggered grid of arbitrary size, J. Comput. Phys. 20 (1976) 171–182.
[30] P.N. Swarztrauber, The methods of cyclic reduction, Fourier analysis and the FACR algorithm for the discrete solution of Poisson's equation on a rectangle, J. Comput. Phys. 19 (1977) 490–501.
[31] R.B. Wilhelmson, J.H. Ericksen, Direct solutions for Poisson's equation in three dimensions, J. Comput. Phys. 25 (1977) 319–331.
[32] J. Kim, P. Moin, Application of a fractional-step method to incompressible Navier–Stokes equations, J. Comput. Phys. 59 (1985) 308–323.
[33] M.-J. Ni, R. Munipalli, N.B. Morley, P. Huang, M.A. Abdou, A current density conservative scheme for incompressible MHD flows at a low magnetic